Chapter 5

Band alignment 2D/2D heterojunction for excellent sunlight-driven photo catalytic dye degradation

Engineering two-dimensional (2D) heterostructure using proximitized interfaces is an efficient approach to attain high efficiency photocatalytic performance toward the degradation of dyes. In this chapter, we have discussed the development of 2D/2D g-C_3N_4/CuSe heterostructure as smart photocatalyst to degrade methylene blue (MB) dye under sunlight. Synergistic effect of 2D layered constituents in heterostructure with strong interfacial interaction and abundant coupled interfaces facilitate efficient charge separation contributing to the high photocatalytic activity. This chapter basically elaborates on 2D/2D face to face contact heterostructures as a photocatalyst for quick and rapid degradation of dye. Moreover, the chapter is divided into two parts: Part A and Part B. Part A consist of experimental and Part B theoretical analysis.
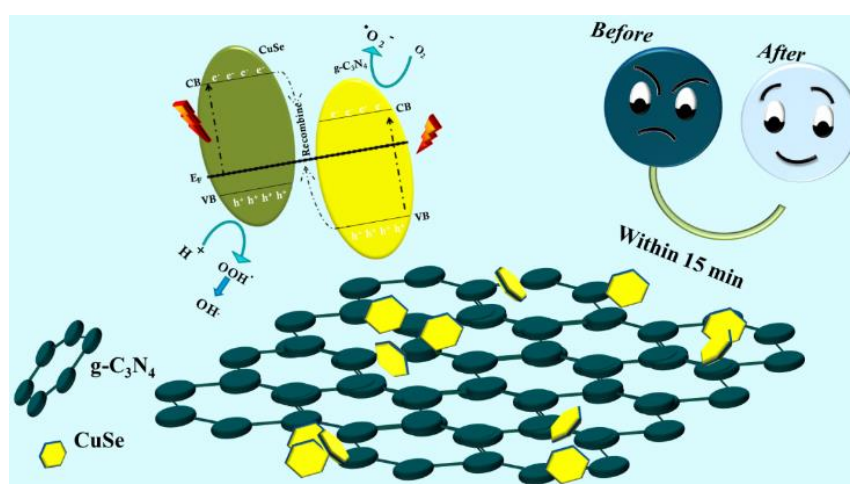

Figure 5.1: Schematic representation of interaction between 2D/2D vdW heterostructure with localized charge distribution for efficient dye degradation.

5.1 Introduction

Rapid increase in industries and numerous anthropogenic activities result in contamination of potable water, solemn problem across worldwide. Among various pollutants, dye migration into the water is a subject of concern from toxicological viewpoints. The extensive use of various dye elements by manufacturing companies and dumping those pollutants directly into water affects the ecosystem [1,2]. Dyes and their by-products gradually destruct and interrupt the aquatic ecosystems by changing the chemistry of water. It not only influences the aquatic flora and fauna, but also misbalances the photosynthetic processes of aquatic plants. Organic dyes bear numerous applications in textile and food industries with certain expected threat to the environment, aquatic and human life because of the non-biodegradable, toxic and carcinogenic aspect [3]. Various industries across the world discharge untreated dyes products which causes severe damage to the environment. Methylene blue (MB) is one of the most common aromatic-cationic dyes of synthetic origin, which causes various harmful effects on animals and human being. Traditional technologies could not meet the required efficiency limit for providing adequate safe water. Therefore, development of advanced materials and methods for photocatalysis with minimum doses yet high efficiency is the urgent need to overcome the rapid increase in water pollution [4]. Sunlight-driven photocatalysts are in focus now days in order to reduce the pollutants. In fact, the target has been focused on promoting the efficiency of catalysts to cater the demand of large-scale industrial applications. Variety of inorganic semiconductor materials has been explored as photocatalysts for water purification under UV or visible light illumination. Therefore, using maximum solar spectrum (43% of the visible light), visible light-sensitive semiconductor photocatalysts can be developed for the degradation of toxic dyes in wastewater management. Copper selenide (CuSe), a *p-type* semiconductor has been used in solar cells, optical filters, superionic materials etc. The stoichiometric (Cu_2Se, Cu_3Se_2, etc.) and non-stoichiometric ($Cu_{2x}Se$) phases of copper selenide has been studied for various dye removal.

In practice, CuSe exhibits visible-light absorption ability due to its narrow bandgap in the range of 1.4-2.2 eV, which is suitable for the photocatalytic process [5]. However, due to high recombination rate and poor migration capability of photogenerated electrons, the large-scale applications are still limited. As a typical metal-free semiconductor with bandgap ~2.7 eV, graphitic carbon nitride (g-C$_3$N$_4$) structure, similar to graphite, exhibiting good electrical conductivity, large surface area, and high thermal/chemical stability, has attracted growing interest in various applications. However, due to quantum size effect, the photoresponsive range of this material becomes narrow, which somehow hinders its full utilization as photocatalysts. One way to overcome this drawback of broadening the photoresponsive range of photocatalysts and assisting the charge transfer is by creating heterojunctions [6]. In this case, direct face-to-face contact of two different 2D systems i.e., known as 2D/2D heterostructure leads to efficient separation and low recombination rate of photogenerated electron-hole pairs due to its large interfacial area between the two types of nanosheets. The high photocatalytic activity is expected due to high surface area-to-volume ratio, a wide adsorption range of visible light and a low recombination rate of carriers [7]. As type-II heterojunctions contain two semiconductors with small and wide band gaps, where one holds more negative conduction band value, thus allowing the small-band-gap semiconductor to act as a sensitizer. Moreover, advantages of type-II heterojunction are that it can eventually enable easy electron transfer to the conduction band of the wide-band-gap semiconductor [8].

In this chapter, development of a type-II 2D/2D heterostructure (shown in **Figure 5.1**) composed of CuSe (*p-type* semiconductor) and g-C$_3$N$_4$ (*n-type* semiconductor), will be discussed which indicates its possibility in removal of environmental pollution. Generally, the photocatalytic property of the developed heterostructure is related to its constituent components, surface area and heterojunction interface. To support the experimental findings, we incorporate density functional theory (DFT) based *ab initio* simulation on gC$_3$N$_4$/CuSe

heterostructure system to realize the electronic properties and charge density map with MB presence.

5.2 Methods and Methodology

Part A

5.3 Experimental

5.3.1 Chemicals and materials used

Precursors like, Selenium dioxide, Oleylamine, Copper (II) acetate, monohydrate, Urea (CH_4N_2O), Ethanol (C_2H_6O), Sodium borohydride ($NaBH_4$, Â ≥98%) has been procured from Merck, India for synthesis. Double distilled water was used for washing purposes during the synthesis process. The experiments were repeated for three times to achieve the uncertainties in the results.

5.3.2 Synthesis of 2D/2D gC_3N_4-CuSe heterostructure

The synthesis of 2D/2D heterostructure was carried out in our previous chapter i.e. in Chapter 4.

5.4 Results and discussion

5.4.1 Structural and morphology studies

Micro-structural study of the composite was carried out through x-ray diffraction (XRD). **Figure 5.2** shows the XRD pattern of 2D/2D $g-C_3N_4$/CuSe heterostructure. The lattice planes (100) and (002) are due to $g-C_3N_4$ (JCPDS - 871526) and lattice planes (101), (103), (006), (008), (107), (0010), (1011) and (1012) are due to presence of CuSe (JCPDS - 340171) incorporated with $g-C_3N_4$. XRD pattern of $g-C_3N_4$@CuSe reveals the presence of both $g-C_3N_4$ and CuSe in the sample. The prominent signals of the individual peaks of $g-C_3N_4$ and CuSe in the composite endorsed the formation of 2D/2D heterostructure.
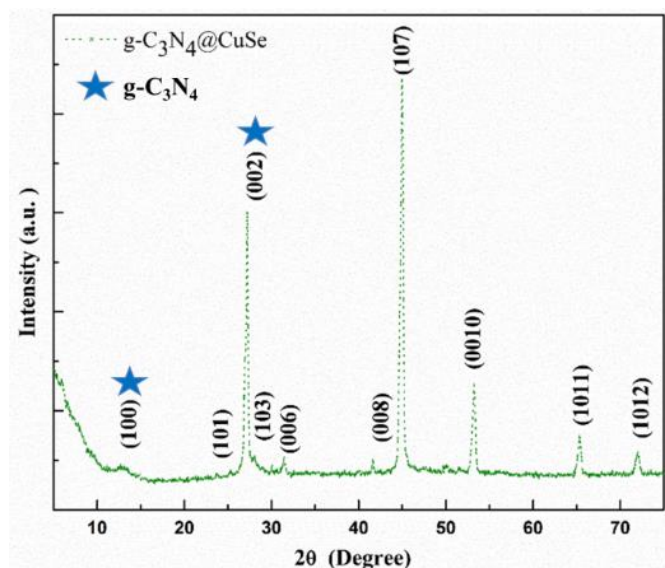
Figure 5.2: X-ray diffraction analysis of g-C_3N_4/CuSe heterostructure.

Figure 5.3 shows the FESEM images of **(a)** bare CuSe and **(b)** 2D/2D g-C_3N_4@CuSe heterostructure. Hexagonal nanoflakes morphology for CuSe were developed using hydrothermal method. FESEM micrographs of g-C_3N_4/CuSe heterostructure with layered morphology of g-C_3N_4 containing wrinkles, where the layers of g-C_3N_4 are covered with agglomerated and accumulated plates of CuSe. Irregular agglomerates of small plates can be identified due to the presence of CuSe nanoflakes (**Figure 5.3 c**). The irregular and rough surface of heterostructure will help in enhancing the degradation capacity for the dye molecules, further accelerating the photocatalytic activity. Thus, the close interface created between g-C_3N_4 and CuSe will help in accelerating the separation of photo excited carriers in the degradation process. Further the images reveal the 2D/2D heterojunction with intimate coupling between (2D) g-C_3N_4 and (2D) CuSe. Here, we notice the formation of 2D/2D g-C_3N_4/CuSe system from the microscopy studies. We support geometry optimization related DFT simulation results to realize the structural stability and surface free energy of formation of the heterointerface with a close proximity to our experimental morphological analysis.
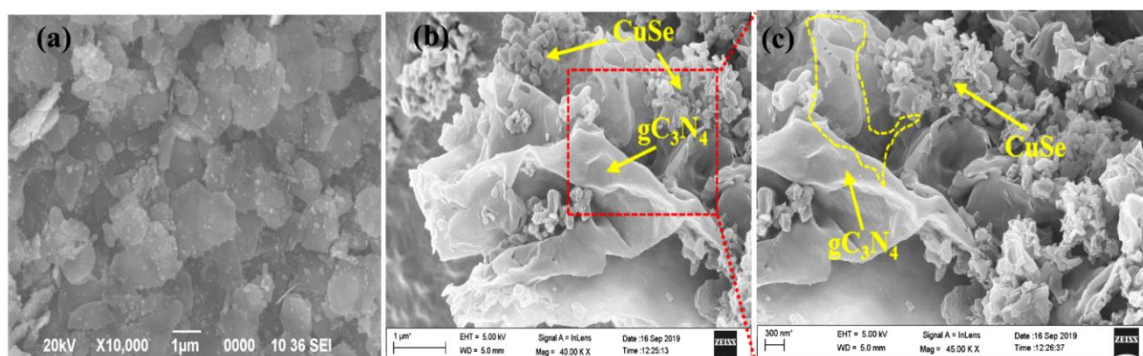
Figure 5.3: (a) SEM images of CuSe nanoflakes and **(b)** g-C$_3$N$_4$/CuSe heterostructure **(c)** Zoomed version of the selected area in red dotted line. Yellow dotted line shows the interfaces formed between g-C$_3$N$_4$ and CuSe.

To obtain a clear insight into the interface between g-C$_3$N$_4$ and CuSe, morphology and detailed microstructure of the heterojunction was investigated by transmission electron microscopy (TEM). The typical TEM (**Figure 5.4 a-c**) image shows clear and ordered lattice fringes, with a lattice spacing of ~0.34 nm corresponding to (101) crystal plane of CuSe nanoflakes exhibiting the coupling of CuSe nanoflakes with g-C$_3$N$_4$ sheets (**Figure 5.4 a**). Further interfaces of CuSe nanosheets on the surface of g-C$_3$N$_4$ nanosheet are clearly observable in **Figure 5.4 (b and c)** which leads towards effective photogenerated charge separation and transfer within the heterojunction.
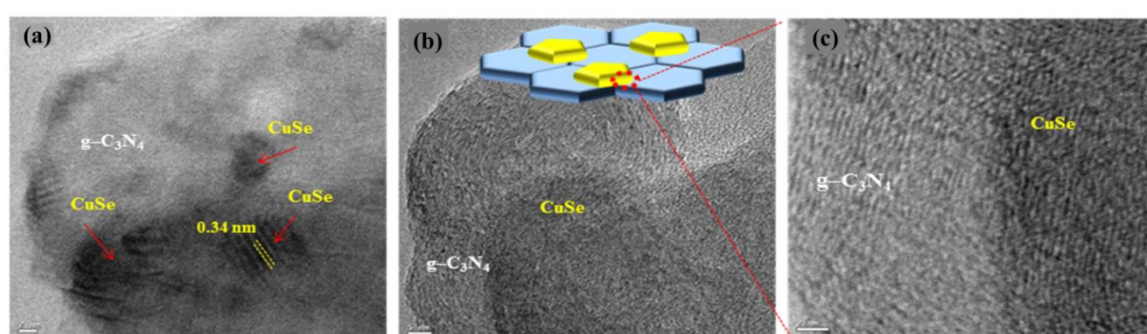

Figure 5.4: (**a and b**) HRTEM images of g-C$_3$N$_4$/CuSe heterostructure (**c**) Zoomed version of the selected area in red dotted line which identifies the formation of the heterointerface.

5.4.2 Spectroscopy Analysis

Raman spectrum, performed using 514 nm wavelength as shown in **Figure 5.5,** identifies the constituents of the product present in the heterostructure. The most intense peak centered at 256.7 cm^{-1} is attributed to stretching mode of Cu-Se bond of klockmannite CuSe. 576 cm^{-1} signifies second longitudinal optic phonon mode of CuSe nanoflakes. Moreover, Raman spectrum of g-C$_3$N$_4$@CuSe shows two peaks that are referred to as G band (1536 cm^{-1}) assigned to ordered graphite carbon and D band (1339 cm^{-1}) assigned to disordered graphite carbon. The G band frequency becomes redshifted, and the D band peak is slightly blue shifted after the formation of the heterostructure which further confirms the formation of more domains of g-C$_3$N$_4$. The I$_D$/I$_G$ intensity ratio of the heterostructure was found to be 0.87, which is higher than the pristine g-C$_3$N$_4$, corresponds to an ordered graphite carbon structure. Thus, increment in I$_D$/I$_G$ ratio is credited to formation of sp^2 domains, during the formation of heterostructure. Moreover, 445 cm^{-1} peak was due to CN heterocycles. 789 cm^{-1} peak was due to bending mode of s-triazine. 1438 cm^{-1} peak was assigned to β(CNC). 892 and 1184 cm^{-1} peak were assigned to ν(CN) mode. 691 cm^{-1} peak was assigned to β (NCN) and ν(CN) mode on ring atoms.

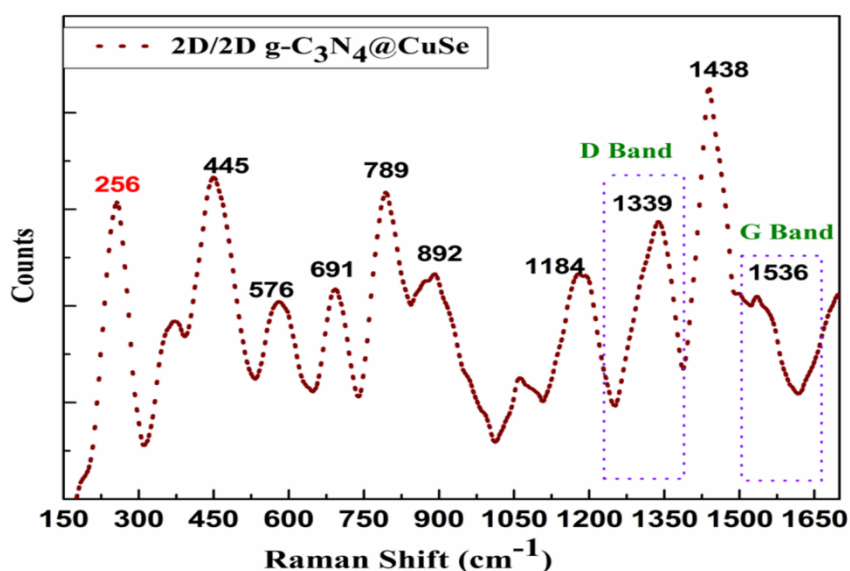**Figure 5.5:** Raman spectrum of 2D/2D g-C$_3$N$_4$/CuSe heterojunction.

Figure 5.6 represents the UV visible characteristics of CuSe, g-C$_3$N$_4$ and 2D/2D heterostructure. It can be seen that the absorption spectra of g-C$_3$N$_4$ (**Figure 5.6 (b)**) and 2D/2D heterostructure (**Figure 5.6 (c))** are similar, but CuSe **(Figure 5.6 (a))** is quite different from the two. The band edges of CuSe and g-C$_3$N$_4$ are 300 nm and 397 nm, indicating that UV activity of the two is relatively significant. Whereas, the absorption edge of 2D/2D g-C$_3$N$_4$@CuSe reaches 402 nm. Therefore, introducing CuSe nanoflakes into g-C$_3$N$_4$ further helps in promoting the Frenkel exciton dissociation, widening the visible light response range. Compared with the optical absorption spectrum of individual CuSe and g-C$_3$N$_4$ nanomaterials, 2D/2D heterojunction absorption spectrum shows significant red shift which is important for strengthening the heterojunction's photocatalytic activity. Thus, development of 2D/2D heterointerface further helps in charge separation and transport which overall enhances the charge transfer mechanism. Moreover, the redshift from UV graph justifies the metallic nature of the heterostructure which is corroborating with the theoretical analysis. The band gap energies of CuSe, g-C$_3$N$_4$ and 2D/2D g-C$_3$N$_4$@CuSe are estimated to be 1.8 eV, 2.4 eV, and 0.77 eV, respectively. This proves that the heterostructure band gap becomes smaller after compositing with g-C$_3$N$_4$, and the photocatalytic effect gets enhanced.
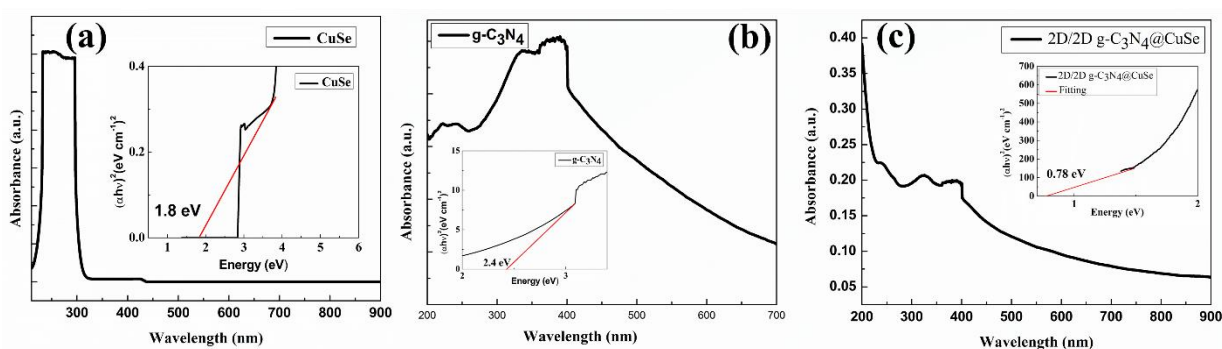

Figure 5.6: UV-vis diffuse reflectance of **(a)** CuSe, **(b)** g-C$_3$N$_4$ and **(c)** 2D/2D g-C$_3$N$_4$/CuSe heterojunction. Inset showing the band energies of respective systems.

Figure 5.7 shows the room temperature photoluminescence spectroscopy (PL) result excited at 405 nm wavelength of g-C_3N_4 **(Figure 5.7(b))**, 350 nm of CuSe (**Figure 5.7(a))** and 280 nm of 2D/2D heterostructure. In case of heterostructure (**Figure 5.7(c))**, the system indicates an emission peak at 435 nm which is due to 2D g-C_3N_4 nanosheets. Further, emission peak observed at 525 nm indicates presence of intrinsic point defects which are usually found at the surface of CuSe. Moreover, the fluorescence emission of g-C_3N_4 gets quenched during the formation of heterostructure which suggests that there is a strong interaction between both 2D semiconductors which may lead to formation of heterojunction and to enhanced charge separation of the photoexcited charges due to new nonradiative recombination paths.
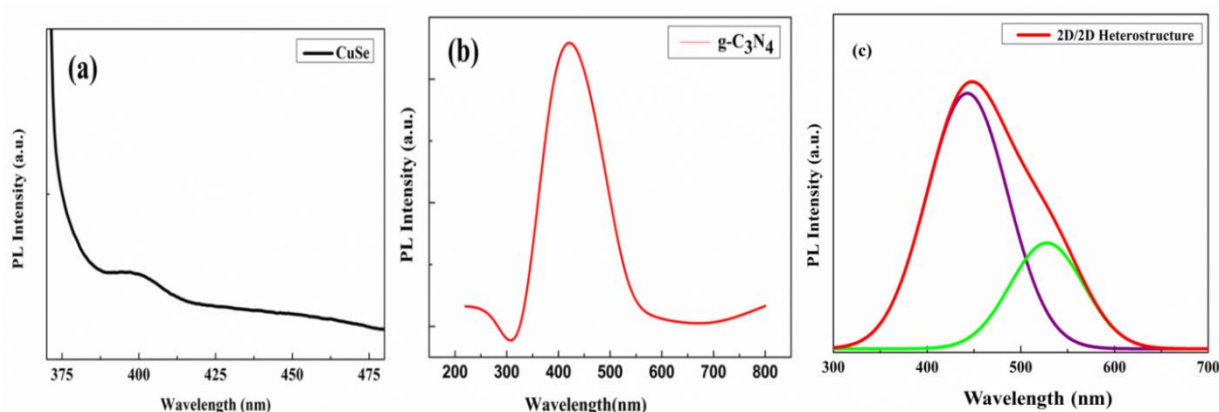

Figure 5.7: Photoluminescence spectra of **(a)** CuSe, **(b)** g-C_3N_4 and **(c)** 2D/2D g-C_3N_4/CuSe heterojunction.

5.4.3 Photocatalytic activity

Figure 5.8 (f) shows the mechanism for photocatalytic degradation of MB using 2D/2D g-C_3N_4@CuSe heterostructure. As directed by their band gap energies, both C_3N_4 and CuSe are active in visible light. When the developed g-C_3N_4@CuSe heterostructure catalyst is exposed to visible light, electrons from the valence band (VB) of CuSe and g-C_3N_4 gets excited to individual conduction bands (CB). Electrons from CB of g-C_3N_4 moved towards the CB of CuSe, which results in formation of free $O_2^{\bullet-}$ radicals. This formation might directly oxidize and break

the pollutant molecule or may further convert water molecules to HO•, which lead towards oxidization of the pollutants to form degraded products. Simultaneously reaction between the VB of g-C_3N_4 with H_2O also occurs, which lead towards the formation of oxidative species such as HO•, oxidizing the dyes to form other degraded less harmful products or CO_2 and H_2O. The visible-light photocatalytic activity of the sample was studied by the degradation of MB dye under sun light. In order to perform the analysis, an added catalyst dose 0.02 g/L with 100 mL volume of methylene blue (MB) dye solution (initial concentration=60 mg/L, pH=7 and temperature 35^0C) was prepared, where 200 mg sodium borohydride ($NaBH_4$) was added for fast kinetics and good stability. After sonication, the solution was placed under sun light. The photocatalytic degradation of MB dye was investigated through time variation with the aid of UV-vis spectrophotometer (**Figure 5.8(e)**). Presence of porous nature within the system further enhances the photocatalytic activity due to their high contact area with the organic dye. Apart from synergistic effects of the individual component in the developed heterostructure, presence of oxygen-containing functional groups and aromatic sp^2 domains allow g-C_3N_4 to contribute in a wide range of bonding and interactions. Complete decolourization of MB dye takes place within 15 min (**Figure 5.8 (a-d)** real time images) for the as prepared g-C_3N_4/CuSe heterostructure. It can be seen from the graph that absorbance intensity and concentration of dye decreases with respect to time due to presence of 2D/2D g-C_3N_4/CuSe in the solution. The phenomenon behind degradation of MB by the developed heterostructure could be via electrostatic interactions and hydrogen bonding between carboxyl or hydroxyl surface groups of g-C_3N_4. Further interaction between the aromatic rings of the dye with π electrons of g-C_3N_4 through π-π electron coupling helps in achieving high efficiency of dye degradation [9]. It shows that the g-C_3N_4/CuSe heterostructure significantly enhanced the photocatalytic efficiency for MB dye removal under sunlight. In order to calculate the percentage of dye degradation, aliquots were taken at regular interval of time and were analysed in a UV-Vis spectrophotometer to

measure the absorbance. Degradation was calculated as per the Eqn. 1 given below.

$$\% \text{ of Degradation} = (C_0 - C_e)/C_0 \times 100\% \ldots\ldots\ldots\ldots\ldots\ldots\ldots(1)$$

where C_0 is the MB concentration at initial state and C_e is the MB concentration after illuminating sun light exposure. 80% dye was degraded within 15 minutes. It is observed that the characteristic peak at 664 nm decreased abruptly with prolonging the contact time, which strongly indicates the selective adsorption of MB in the mixed dye solution by the developed heterostructure system. The main mechanism behind the degradation is mainly due to enhanced charge carrier transport, improved crystallinity and reduced charge transport resistance within the system. The crucial properties of the system that affect the degradation efficiency are relatively the high surface area with large number of active sites which help in leading high-capacity adsorption [10].
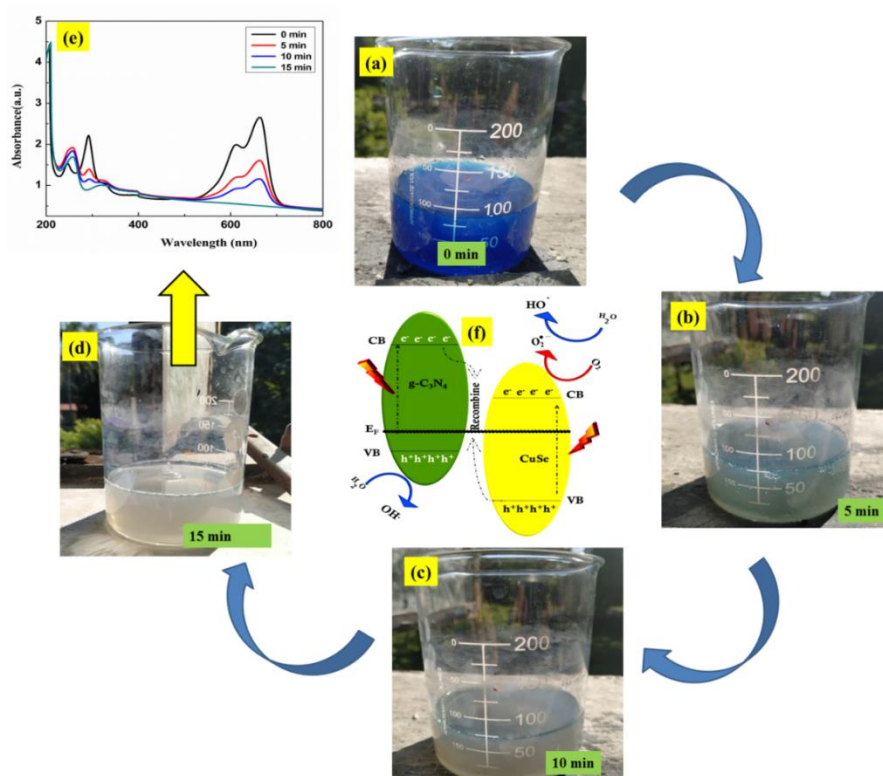

Figure 5.8: (a-d) Identifies the Real Time Images of MB dye removal under sun light exposure, **(e)** Investigation of Photo degradation of MB using 2D/2D heterostructure under UV-vis absorbance spectrum taking different time interval. **(f)** Mechanism showing the removal of dye using 2D/2D heterostructure.

5.4.4 Kinetics and Surface Charge analysis

Photocatalytic oxidation of organic pollutants follows first-order kinetics. The linear relationship between $\ln(C_0/C_t)$ and Time shown in **Figure 5.9 (a)** confirms that the photocatalytic degradation procedure of MB followed the apparent pseudo-first-order which is expressed as the Eqn. 2 given below;

$$\ln(C_0/C_t) = kt \dots\dots\dots\dots\dots\dots\dots\dots\dots\dots\dots(2)$$

where, k is the apparent pseudo-first-order rate constant, C_0 and C_t are the initial and remaining dye concentration in aqueous solution at time t. The slope of the linear plot of pseudo first order graphical presentation estimates apparent rate constants for the degradation process and was found to be 0.107 min^{-1} for the developed heterostructure. The zeta potential values of the developed 2D/2D heterostructure in water were measured at five different pH range (as shown in **Figure 5.9 (b)**) to explore the magnitude and characteristics of surface charge density around the heterostructure. Over the entire pH range, it was negatively charged, which enhances with increasing pH. The reason behind negative charge is due to the ionization of functional groups (carboxylic and/or hydroxyl) on the sheets of $g\text{-}C_3N_4$. Since, CuSe nanoflakes were immobilized on $g\text{-}C_3N_4$ nanosheets, the developed heterostructure had greater negative charge indicating more stable behaviour of the heterostructure [11].
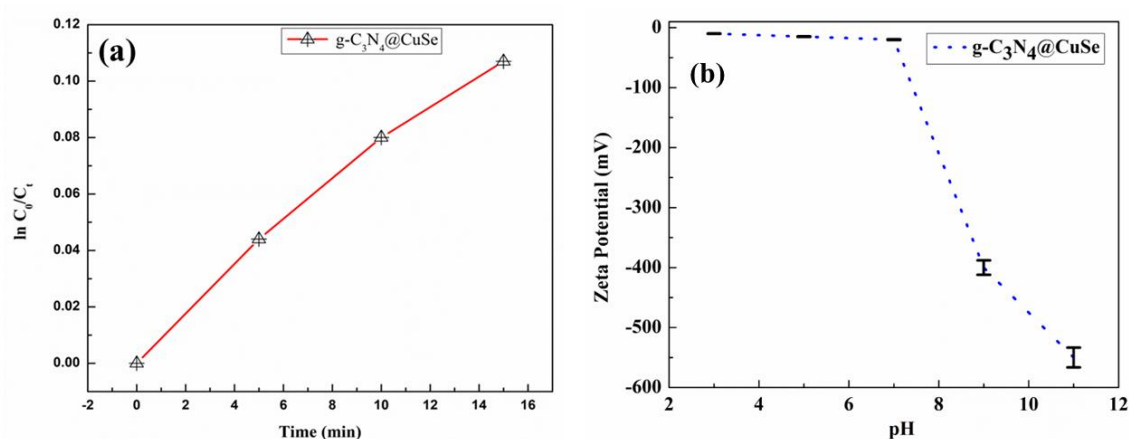

Figure 5.9: (a) Kinetics and **(b)** Zeta potential for dye degradation.

Part B

5.5 Theoretical Analysis

5.6 Computational Set-up

The geometry optimization and electronic structure calculations of the van der Waals (vdW) heterostructures are performed by using the projector augmented wave formalism [12] based on DFT simulation, as implemented in the QUANTUM Espresso package [13]. The PerdewBurke-Ernzerhof (PBE) generalized-gradient approximation (GGA) is generally used to describe the exchange and correlation functional.[14] Some aspects of the calculations related to band alignments, simulations have been performed using the plane wave projected augmented wave (PAW) method as implemented in Vienna *ab initio* Simulation Package (VASP) code [15]. Here, we use the semi local exchange-correlation functional like PBE,[16] semilocal meta-GGA case (MGGAC) [17]. Unlike GGAs, the meta-GGA functional MGGAC can be implemented in generalized KS (gKS) [18] scheme because of the dependence of the *KS* orbital. MGGACs are quite reliable than GGAs to recognized the covalent, metallic, and non-covalent interactions[18] Meanwhile, the GGA approach usually underestimates the band gap of semiconductors, we use the screened hybrid functional of Heyd-Scuseria-Ernzerhof (HSE) [19] for a more accurate description of the electronic structure. In this work, we use the HSE06 functional [19] with a screening parameter ω = 0.20 Å^{-1} and a small mixing parameter α (α = 0.175) for the short-range Hartree-Fock exchange instead of the commonly used value of 0.25. Here, the system is considered to be semiconducting graphitic carbon nitride (g-C_3N_4) and semiconducting copper selenide (CuSe) to form g-C_3N_4/CuSe heterostructure system. Next, we have assembled one dye called as Methylene Blue (MB) containing C, N and S atoms. Thus, in total, two (i.e. g-C_3N_4/CuSe and g-C_3N_4/CuSe-MB) heterostructures are considered respectively, here for simulations. To describe well the Cu *3d* electrons, the GGA+U method is especially employed for them,[20] in which the effective *on-site* Coulomb interaction (*U)* and exchange interaction (*J)* are set to be 3.0 and 0.9 eV,

respectively. For the isolated system of gC$_3$N$_4$-CuSe-MB, more accurate and effective functional have been used to achieve the optimized geometry structures and electronic states. The plane-wave cut off energy is set to be 480 eV and a vacuum space of larger than 12Å is used to avoid the interaction between two adjacent slabs. The 9× 9×9 and 27× 27×27 Monkhorst-Pack grids are set for the heterostructure system for optimization and density of states calculations, respectively, to conduct the first Brillouin zone integration. The vdW corrections with Grimme (DFT-D2) method are considered in the calculations.

5.6.1 Electronic Structure Studies

Detailed electronic structure properties (i.e. density of states (DOS) with their respective orbital reciprocal *k-space* projections and charge density distribution) are analysed subsequently to realize the accurate internal mechanism of the photocatalytic response of the systems. Densities of states (DOS) shown in **Figure 5.10 (a) and (b)** for g-C$_3$N$_4$/CuSe and g-C$_3$N$_4$/CuSe-MB, respectively have been plotted to understand the origin and control of molecular motion for material activity of the active sites formed in the g-C$_3$N$_4$/CuSe heterostructure system. Overlapping electronic states are clearly observed from the DOS plots showing the dynamic and metallic nature persisting in the systems. Here, activity of Cu and Se atoms preserve the metallicity with overlapping states around the Fermi level. As a result, all electrons localised over g-C$_3$N$_4$ surface and achieve overlapping states at the Fermi level within the conduction band and improved kinetic energy showing delocalized nature of the active metal sites.
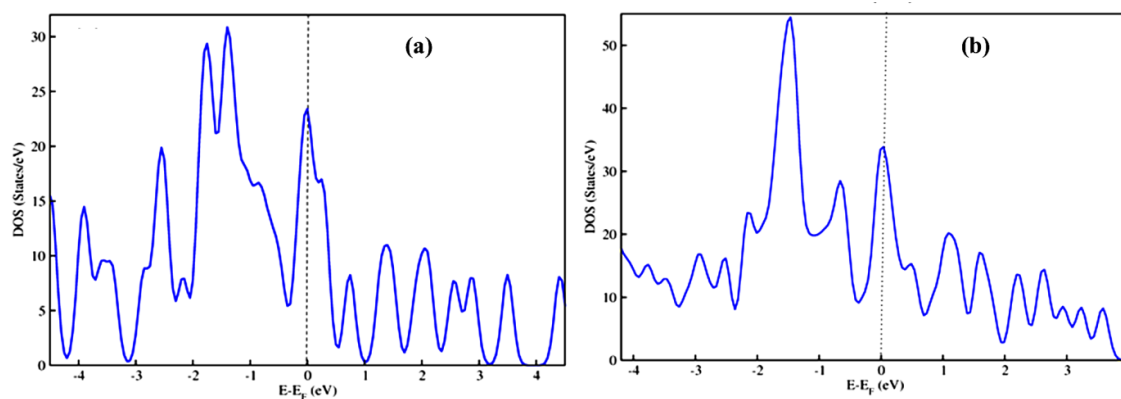
Figure 5.10: Density of States (DOS) plot for **(a)** g-C$_3$N$_4$/CuSe and **(b)** g-C$_3$N$_4$/CuSe-MB are shown.

5.6.2 Charge Density

The charge density profile of g-C$_3$N$_4$/CuSe (**Figure 5.11 (a)**) and g-C$_3$N$_4$/CuSe-MB (**Figure 5.11 (b)**) heterostructure is mapped. It is obvious that CuSe prevails semiconducting nature with a finite bandgap, while the pristine g-C$_3$N$_4$ is also a semiconductor with finite bandgap. Hence, the heterostructure system has a distinctive metal-semiconductor associated characteristic. It can be observed that there is rare motion of charge carriers due to the vdW interaction between the two systems, but localised charge distribution on the surface of g-C$_3$N$_4$/CuSe heterostructure is noticed to some extent. Strong proximity synergy among the Cu, Se atoms with C, N atoms shows that the interface coupling effect is mostly dependent on the orbital hybridization at the interface of the heterostructure. The blue regions show the localization of electrons in the core (**Figure 5.11 (a)**). While, delocalised nature is clear on the g-C$_3$N$_4$/CuSe system in presence of MB attachment (**Figure 5.11 (b)**), supporting the improved kinetic energy persistent in the MB attached heterostructure with higher molecular motion leading to electron delocalization behaviour.
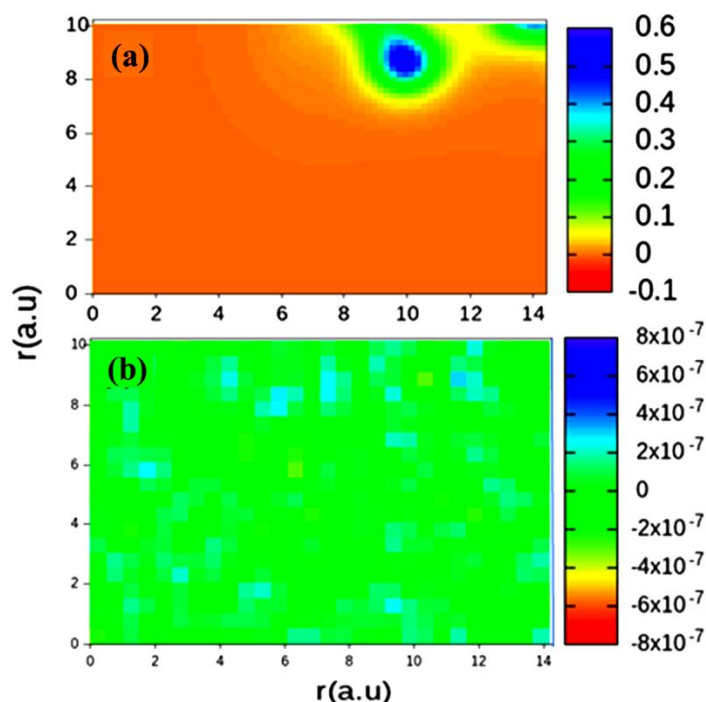
Figure 5.11: Electronic Charge density counter maps have been plotted for **(a)** g-C₃N₄/CuSe and **(b)** g-C₃N₄/CuSe-MB with scale bar.

5.6.3 Atomic Orbital Projection Analysis

The contribution of *p* orbitals of C, N, Se and S atoms and *d*-orbitals of Cu atoms are indicated by the local density of states (LDOS) mapping, where C_p, N_p, Se_p, S_p and Cu_d orbitals are more intense. **Figure 5.12 (a)** shows the LDOS mapping of g-C₃N₄/CuSe heterostructure, whereas **Figure 5.12 (b)** shows the same for g-C₃N₄/CuSe-MB heterostructure. The DOS pattern is projected in reciprocal *k-space* to get projected density of states (PDOS). Here, atomic orbitals for both g-C₃N₄/CuSe (shown in **Figure 5.13 (a-d)**) and g-C₃N₄/CuSe-MB (shown in **Figure 5.13 (e-i)**) systems have been resolved. The PDOS pattern clearly indicates the reflection of all atomic orbitals of the constituent atoms (i.e. C, N, Cu, Se and S) with MB attachment and without attachment of the systems. It is noticed that there is no improvement in projection densities of the systems in both cases confirming the existence and equal contribution with overall projection of all atomic orbitals that are present in the heterostructure systems. The PDOS pattern

shows the orbital splitting behaviour supporting the respective electronic charge density mapping.
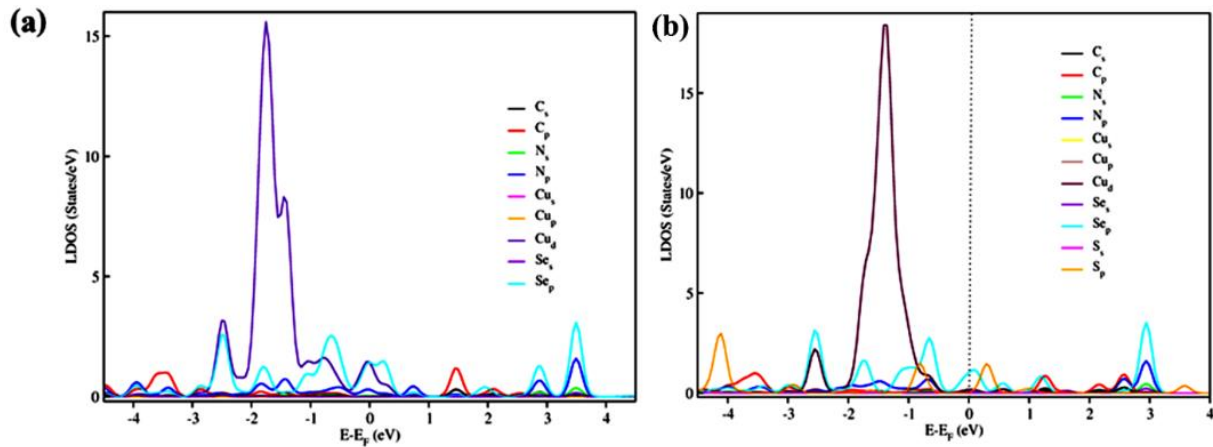

Figure 5.12: Local density of states (LDOS) plot for **(a)** g-C$_3$N$_4$/CuSe heterostructure and **(b)** g-C$_3$N$_4$/CuSe-MB heterostructure.

We note that equal distribution of atomic orbital in these PDOS plot indicates an overlapping metallic stage. For accurate prediction of electronic PDOS pattern, we have implemented *U* and *J* parameter in the simulation with varying functional and vdW corrections. This can be attributed to the effect of the Cu metal atoms on g-C$_3$N$_4$ sheet substrate to retain the metallic nature in the heterostructure system. Carbon, Nitrogen and Sulphur atomic orbitals show significant states which are delocalized in the heterostructure system.
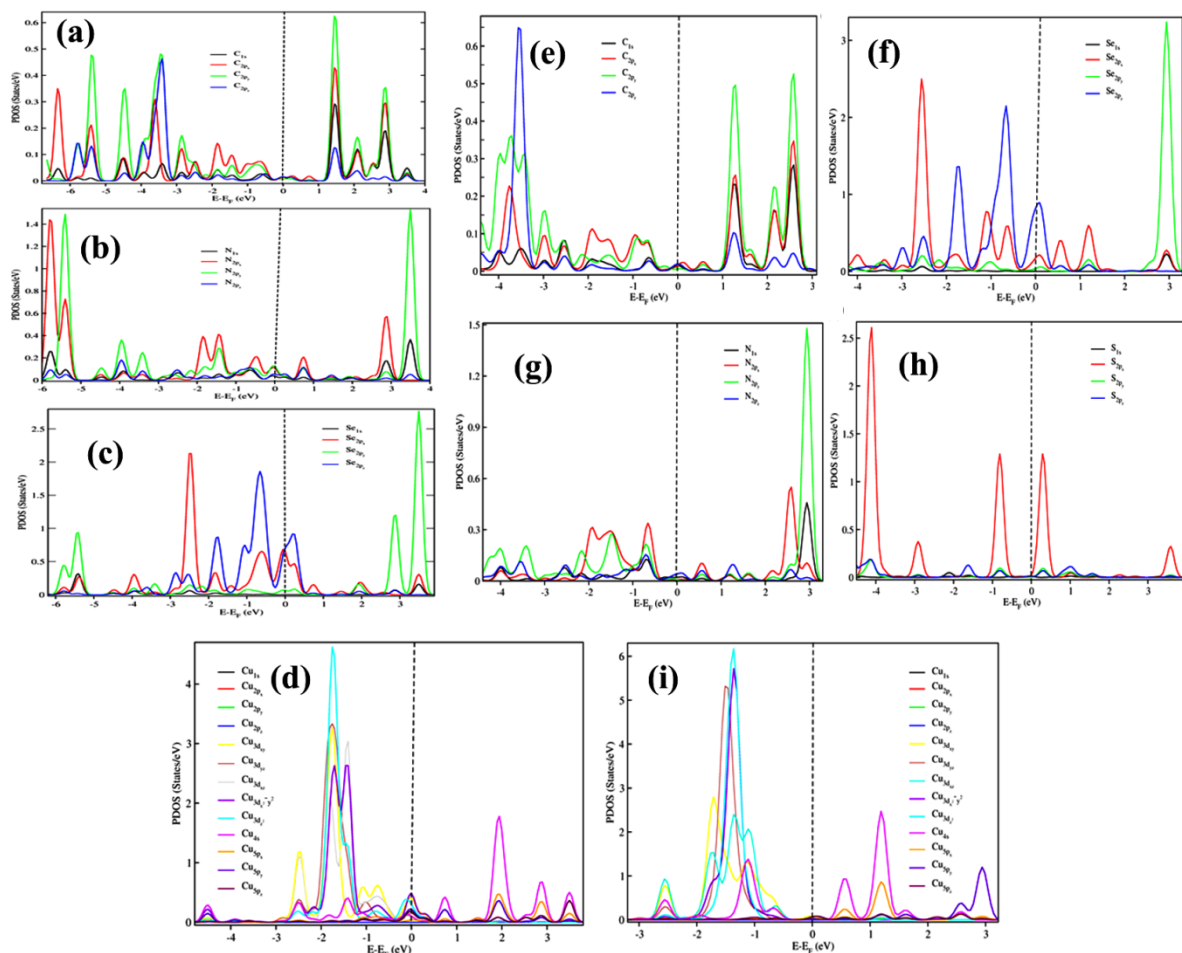
Figure 5.13: Projected density of states (PDOS) of individual atoms **(a)** C **(b)** N **(c)** Se and **(d)** Cu for g-C$_3$N$_4$/CuSe heterostructure and **(e)** C, **(f)** N, **(g)** Se, **(h)** S and **(i)** Cu for g-C$_3$N$_4$/CuSe-MB heterostructure are plotted.

5.6.4 Investigating the Band Alignment

The prime reasons behind the occurrence of efficient photocatalytic dye degradation are as follows- Firstly, exciton of electrons from valence to conduction band due to absorption of photons. Secondly, recombination of electron holes within the surface or the interfaces of the system. And thirdly, during the whole process, the electron and hole which do not get under recombination, indulges in occurrence of oxidation and reduction reaction with the surrounding adsorbents. The *p-type* behaviour of CuSe and *n-type* behaviour of g-C$_3$N$_4$ ultimately combines to form a *p-n* heterojunction as shown in **Figure**

5.14, where at the interface electron transfer occurs from *n-type* to the *p-type* part. The mechanism behind the brilliant performance of the photocatalytic activity is the strong electron-hole separation within the interface, where photogenerated electrons transfer from the conduction band (CB) of the *p-type* part to the CB of the *n-type* and holes from valence band (VB) of the *n-type* to the VB of the *p-type*. Electronic band alignment controls the separation of photogenerated carriers, which has been obtained by plotting the PDOS plots (shown in **Figure 5.13**) of the systems across the interfaces. Thus, this calculation is very important in understanding the enhanced photocatalytic behaviour in such heterojunctions especially in nanoscale dimension. Dashed lines in **Figure 5.14** indicate the valence band maxima (VBM) and conduction band minimum (CBM) of the CuSe and g-C$_3$N$_4$ systems, and the resulting band alignment diagrams are shown in **Figure 5.14**. It is clear that the heterostructure bears a type-II band alignment [21,22].
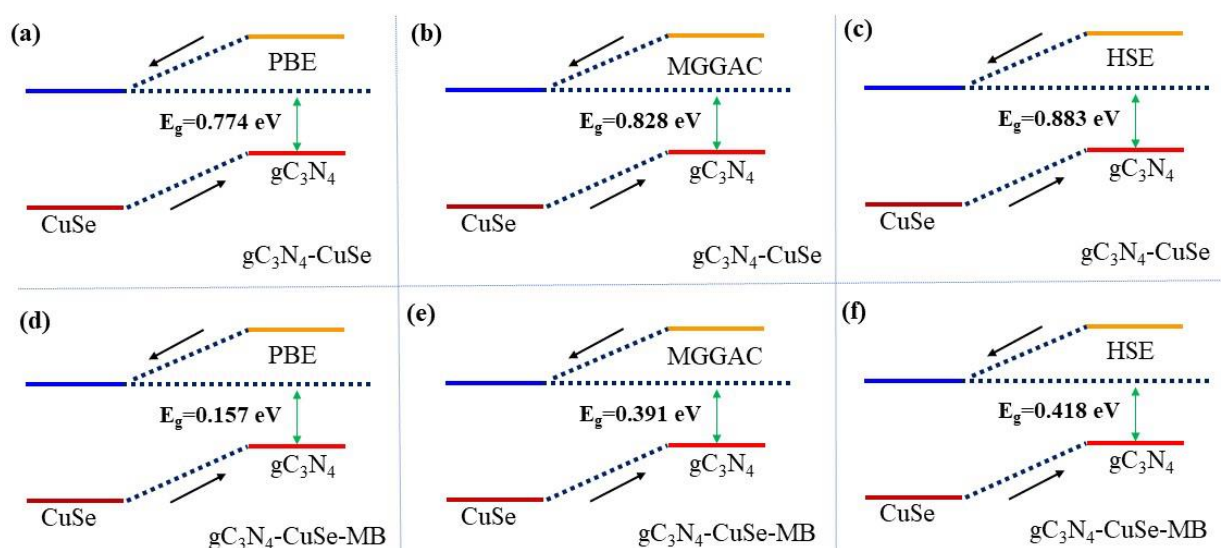

Figure 5.14: Band alignment of the heterojunctions (top panel from (**a-c**)) for g-C$_3$N$_4$/CuSe and (bottom panel from (**d-f**)) g-C$_3$N$_4$/CuSe-MB obtained from PBE, MGGAC and HSE functional, respectively.

Our theoretical simulation results are very much consistent with experimental findings discussed here. For *in-depth* realization, we show the band alignment diagrams calculated using the PBE (**Figure 5.14 (a and d)**), MGGAC (**Figure 5.14 (b and e)**) and HSE (**Figure 5.14 (c and f)**) hybrid functional for g-C$_3$N$_4$/CuSe (**Figure 5.14** (top panel from **(a-c)**)) and g-C$_3$N$_4$/CuSe-MB systems (**Figure 5.14** (bottom panel from **(d-f)**)), respectively. It is clearly observed that the band gaps of the heterostructure are severely underestimated with the PBE functional. The qualitative features of the band alignments are similar to those calculated using the MGGAC and HSE functional. Here, we would like to mention that calculating these band alignments of solids in nanoscale typically involves several steps because of the need to understand the participation of individual atoms on the proximitized hetero interface (shown in **Figure 5.15 (a and b)**) and electrostatic potential line ups (shown in **Figure 5.16 (c and d)**) of the individual solids in any heterojunctions [23]. For finite periodic solid systems, however, band alignments at the hetero interface can be obtained by inspecting the atomically projected states. Therefore, photogenerated lowest energy electrons and holes will be spontaneously separated in this heterojunction, making them suitable for photocatalysis applications and prompt dye degradation.

5.6.5 Intrinsic uncertainty via proximitized hetero interface

The inverse participation ratio (IPR) is an easy technique to quantify the electronic states of individual atoms distributed over a heterointerface in quantum regime (*i.e.* nanoscale dimension) to sort out the intrinsic uncertainty in presence of proximity effect [24]. It is obvious that this type of intrinsic uncertainty arises in quantum regime, because an electronic state can exist in a quantum superposition of states over many positions across the interface. Here, the state of electrons in a bound state of g-C$_3$N$_4$ and CuSe molecule is delocalized over several atomic orbitals. Thus, the IPR results identifies a sensible count for how many atoms is delocalized over, even when the probability distribution is not evenly distributed across the interface strongly supporting our microscopic

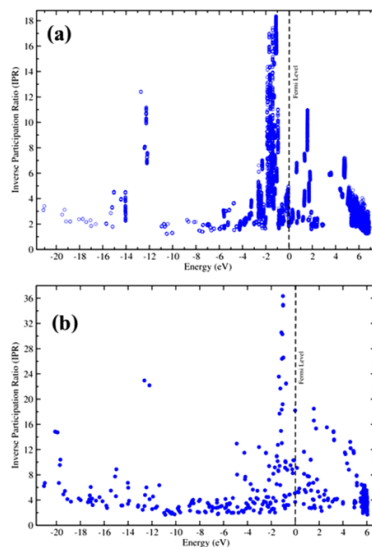FESEM images of unevenly distribution of CuSe over g-C$_3$N$_4$ system in the nanocomposite heterostructure.

Figure 5.15: Inverse participation plots of the heterojunctions for **(a)** g-C$_3$N$_4$/CuSe and **(b)** g-C$_3$N$_4$/CuSe-MB. All the calculations have been performed using HSE functional. Black dotted vertical line presents the Fermi level in **(a)** and **(b)**.
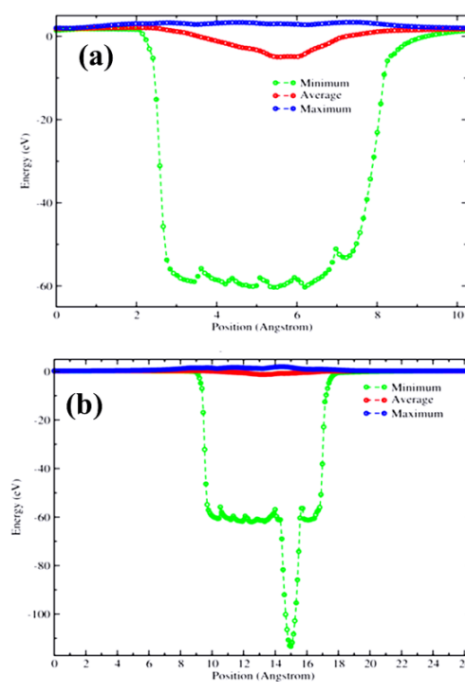

Figure 5.16: Electrostatic potential plots of the system for **(a)** g-C$_3$N$_4$/CuSe and **(b)** g-C$_3$N$_4$/CuSe-MB. All the calculations have been performed using HSE functional.

Figure 5.15 (a) and (b) show the IPR distribution plots for g-C$_3$N$_4$/CuSe and g-C$_3$N$_4$/CuSe-MB, respectively. It is observed from this simulation plot that CuSe atomic states are more unevenly distributed over g-C$_3$N$_4$ surface, indicating unevenly delocalization of electronic states due to the proximity coupling in the g-C$_3$N$_4$/CuSe interface. Similarly, presence of MB in the interface makes charge neutrality, hence creates even distribution of IPR with charge delocalization over the hetero interface. The uneven distribution of electronic states over the interface gives rise to nonzero surface charge and subsequent electrostatic potential due to the accumulation of local potential energy [25] (shown in **Figure 5.16 (a) and (b)**). It is clearly observed from the average local potential energy profile that uneven charge is present in case of proximized g-C$_3$N$_4$/CuSe interface, unlike evenly delocalization of average local potential energy i.e. charge neutrality of the interface due to presence of MB. This evenly distribution confirms the average energy values at zero level with respect to various locations over the interface, indicating complete charge neutrality and dye degradation. These combined analyses of IPR and local potential energy profile show the dye degradation process and delocalization of electronic states over the proximitized hetero interfaces of this nanocomposite g-C$_3$N$_4$/CuSe system.

5.7 Conclusion

In this chapter, we have developed a 2D/2D heterojunction of g-C$_3$N$_4$/CuSe and the natural sunlight driven photocatalytic activity of the aforementioned heterostructure was demonstrated by photocatalytic degradation of MB, where the heterostructure exhibited efficient photocatalytic activity and good stability in degradation of dye. It has been observed that formation of g-C$_3$N$_4$/CuSe heterojunction could suppress the recombination of photogenerated electron-hole pairs efficiently, resulting better photocatalytic activity under sunlight for the degradation of organic dye. Our study provides an in-depth understanding of the heterostructure and the charge generation, separation and transfer processes. Various parameters such as efficient broad spectral absorption, specific surface area, stability and uniformity of the system in this study helped

in understanding the enhanced photocatalytic activities of the heterostructure. Moreover, detailed electronic structure and accurate atomic orbital projected states of the heterostructure system in nanoscale have been performed systematically using PBE, MGGAC and HSE hybrid density functional approach with U and J parameters with vdW dispersion correction. The close proximity of CuSe nanoflakes over g-C_3N_4 surface generates proximitized 2D/2D heterointerface facilitating efficient electron transfer process across the edges. These simulation outcomes show that the heterostructure generates new delocalized electronic states, consequently achieve clear overlapping states at Fermi level and providing 3 times enhancement in kinetic energy of the system. The distinct atomic projected behaviour of the band edge states clearly shows a type-II band alignment in this heterostructure, which is beneficial for the separation of photogenerated carriers for prompt dye removal. Meanwhile, analysis of the inverse participation ratio of individual atoms on the proximitized hetero interface and electrostatic potential energy profiles support the charge neutrality and evenly delocalization of the electronic states for complete dye degradation. The idea, strategy and results in this work imply that the developed 2D/2D heterostructure acts as a promising material for dye degradation and can be used efficiently in depollution technologies.

References

[1] Wang, S., Yang, X., Zhang, X., Ding, X., Yang, Z., Dai, K., and Chen, H. A plate-on-plate sandwiched Z-scheme heterojunction photocatalyst: BiOBr-Bi2MoO$_6$ with enhanced photocatalytic performance. *Applied Surface Science,* 391:194-201, 2017.

[2] Wang, P., Wang, M., Zhang, J., Li, C., Xu, X., and Jin, Y. Shell Thickness Engineering Significantly Boosts the Photocatalytic H_2 Evolution Efficiency of CdS/CdSe Core/Shell Quantum Dots. *ACS Applied Materials & Interfaces,* 9:35712-35720, 2017.

[3] Wang, K., Wu, X., Zhang, G., Li, J., and Li, Y. $Ba_5Ta_4O_{15}$ Nanosheet/$AgVO_3$ Nanoribbon Heterojunctions with Enhanced Photocatalytic Oxidation Performance: Hole Dominated Charge Transfer Path and Plasmonic Effect Insight. *ACS Sustainable Chemistry & Engineering,* 6(5):6682-6692, 2018.

[4] Pradhana, S. S., Konwar, K., Ghosh, T. N., Mondal, B., Sarkara, S. K., and Deb, P. Multifunctional Iron oxide embedded reduced graphene oxide as a versatile adsorbent candidate for effectual arsenic and dye removal. *Colloid and Interface Science Communications,* 39:100319-100326, 2020.

[5] Bell, E. C., Munro, C. J., Slocik, J. M., Shukla, D., Parab, A. D., Cohn, J. L., and Knecht, M. R. Biomimetic strategies to produce catalytically reactive CuS nanodisks. *Nanoscale Advances,* 1:2857-2865, 2019.

[6] Behera, S. K., Bora, M., Chowdhurya, S. S. P., and Deb, P. Proximity effects in graphene and ferromagnetic $CrBr_3$ van der Waals heterostructures. *Physical Chemistry Chemical Physics,* 21:25788-25796, 2019.

[7] Wang, K., Li, J., and Zhang, G. Ag-Bridged Z-Scheme 2D/2D $Bi_5FeTi_3O_{15}$/g-C_3N_4 Heterojunction for Enhanced Photocatalysis: Mediator-Induced Interfacial Charge Transfer and Mechanism Insights. *ACS Applied Materials & Interfaces,* 11:27686-27696, 2019.

[8] Basu, M., Garg, N., and Ganguli, A. K. A type-II semiconductor (ZnO/CuS heterostructure) for visible light photocatalysis. *Journal of Materials Chemistry A,* 2:7517–7525, 2014.

[9] Talukdar, M., Nath, O., and Deb, P. Enhancing barrier properties of biodegradable film by reinforcing with 2D heterostructure. *Applied Surface Science,* 541:148464-148471, 2021.

[10] Nithya, M., Vidhya, S., and Praveen, K. A Novel g-C_3N_4/MnV_2O_6 Heterojunction Photocatalyst for the Removal of Methylene Blue and Indigo Carmine. *Chemical Physics Letters,* 737:136832-136860, 2019.

[11] Kresse, G., and Furthmüller, J. Efficient iterative schemes for ab initio total-energy calculations using a plane-wave basis set. *Physical Review B,* 54(16):11169-11186, 1996.

[12] Blöchl, P. E. Projector Augmented-Wave Method. *Physical Review B,* 50:17953-17979, 1994.

[13] Giannozzi, P., Baroni, S., Bonini, N., Calandra, M., Car, R., Cavazzoni, C., Ceresoli, D., Chiarotti, G., L., Cococcioni, M., Dabo, I., Corso, A. D., Gironcoli, S. d., Fabris, S., Fratesi, G., Gebauer, R., Gerstmann, U., Gougoussis, C., Kokalj, A., Lazzeri, M., Samos, L. M., Marzari , N., Mauri, F., Mazzarello, R., Paolini, S., Pasquarello, A., Paulatto, L., Sbraccia, C., Scandolo, S., Sclauzero, G., Seitsonen, A. P., Smogunov, A., Umari, P., and Wentzcovitch, R. M. QUANTUM ESPRESSO: a modular and open-source software project for quantum simulations of materials. *Journal of Physics: Condensed Matter,* 21:395502-395522, 2009.

[14] Perdew, J. P., Burke, K., and Ernzerhof, M. Generalized Gradient Approximation Made Simple. *Physical Review Letters,* 77:3865-3868, 1996.

[15] Kresse, G., and Hafner, J. Ab initio molecular dynamics for liquid metals. *Physical Review B,* 47:558-561, 1993.

[16] Perdew, J. P., Burke, K., and Wang, Y. Generalized gradient approximation for the exchange-correlation hole of a many-electron system. *Physical Review B,* 54:16533-16539, 1996.

[17] Patra, B., Jana, S., Constantin, L. A., and Samal, P. Relevance of the Pauli kinetic energy density for semilocal functionals. *Physical Review B,* 100:155140, 2019.

[18] Perdewa, J. P., Yang, W., Burke, K., Yang, Z., Gross, E., K., U., Scheffler, M., Scuseria, G., E., Henderson, T., M., Zhang, I., Y., Ruzsinszky, A., Peng, H., Sunl , J., Trushin, E., and Görling, A. Understanding band gaps of solids in generalized Kohn–Sham theory. *Proceedings of the National Academy of Sciences of the United States of America,* 114:2801–2806, 2017.

[19] Heyd, J., Scuseria, G. E., and Ernzerhof, M. Hybrid functionals based on a screened Coulomb potential. *The Journal of Chemical Physics*, 118:8207-8215, 2003.

[20] Liechtenstein, A. I., Anisimov, V. I., and Zaanen, J. Density-Functional Theory and Strong Interations: Orbital Ordering in Mott-Hubbard Insulators. *Physical Review B,* 52:R5467-R5470, 1995.

[21] Shubha, J. P., Adil, S. F., Khan, M., Hatshan, M. R., and Khan, A. Facile Fabrication of a $ZnO/Eu_2O_3/NiO$-Based Ternary Heterostructure Nanophotocatalyst and Its Application for the Degradation of Methylene Blue. *ACS Omega*, 6:3866–3874, 2021.

[22] Marschall, R. Photocatalysis: Semiconductor Composites: Strategies for Enhancing Charge Carrier Separation to Improve Photocatalytic Activity. *Advanced Functional Materials,* 24:2421-2440, 2014.

[23] Nasir, S. N. F. M., Ullah, H., Ebadi, M., Tahir, A. A., Sagu, J. S., and Teridi, M. A. M. New Insights into $Se/BiVO_4$ Heterostructure for Photoelectrochemical Water Splitting: A Combined Experimental and DFT Study. *The Journal of Physical Chemistry C*, 121:6218-6228, 2017.

[24] Walle, C. G. Van de., and Martin, R. M. Theoretical study of band offsets at semiconductor interfaces. *Physical Review B*, 35:8154-8165, 1987.

[25] Clark, T. B. P., and Maestro, A. D. Moments of the inverse participation ratio for the Laplacian on finite regular graphs. *Journal of Physics A: Mathematical and Theoretical,* 51:495003-495028, 2018.

[26] Han, Y., Yang, J.Y., and Hu, M. Unusual strain response of thermal transport in dimerized three-dimensional graphene. *Nanoscale*, 10(11):5229-5238, 2018.